communications materials

A Nature Portfolio journal

Article

https://doi.org/10.1038/s43246-026-01339-y

Evidence of an amorphous intermediate phase during non-classical calcium hydroxide crystallization from cementitious pore solutions

Check for updates

Stefan Kopf [1], Elena Willinger[2], Baohu Wu [3] & Torben Gädt[1]

Calcium hydroxide, a primary hydration product of Portland cement, is undetectable by conventional scattering methods or thermal analysis during the dormant period of cement hydration. Its absence suggests it is either dissolved in the pore solution or present in a non-crystalline state, prompting us to investigate its native state in cementitious pore solutions. Here, we show that conventional transmission electron microscopy detects large (100 nm) amorphous calcium hydroxide spheres, whereas cryo-high-resolution transmission electron microscopy, combined with small-angle X-ray scattering and pair distribution function analysis, reveals that these spheres are absent from the native pore solution after 15 min of hydration. Instead, calcium hydroxide exists as fully solvated ions or ion pairs, alongside tiny (1 nm) metastable gypsum prenucleation clusters. In addition to silicates, sulfate ions inhibit calcium hydroxide nucleation, keeping isolated pore solutions metastable for days at sub-ambient temperatures under inert gas, whereas heating or evaporation triggers the multistage "non-classical" crystallization of calcium hydroxide. Our findings confirm "non-classical" crystallization pathways during early Portland cement hydration, the binder of concrete, the most widely used man-made material.

Calcium hydroxide ($Ca(OH)_2$, portlandite, or CH in cement chemistry notation[1]) is a remarkably versatile inorganic compound and a promising candidate for application in new large-scale construction materials[2,3], as well as for CO_2 capture[4,5]. The nucleation and crystallization of CH is thus of fundamental technological importance for the lime industry and cement hydration[6,7]. Besides calcium-silicate-hydrate (C-S-H), CH is the second most abundant hydration product of Ordinary Portland cement (OPC)[8]. It forms according to Eq. 1 by the reaction of Ca_3SiO_5 (C_3S) with water (H), which leads to the subsequent precipitation of both CH and C-S-H from the supersaturated solution[9,10].

$$C_3S + 5.3H \rightarrow 1.3CH + C_{1.7}SH_4 \quad (1)$$

While C-S-H structures have microscopically been detected as early as 60 s after the start of hydration[11], CH remains undetectable by X-ray diffraction (XRD) or scanning electron microscopy (SEM) during the dormant period[12], even though rare reports exist of detecting small amounts of portlandite in cement pastes within the first hour of cement hydration[13]. CH typically appears only in its characteristic crystalline form toward the end of the dormant period[7,14]. However, if detectable C-S-H structures are formed by the hydration of C_3S during the initial hours of cement hydration, CH must also be present according to Eq. 1[15], provided that the early C-S-H phase adopts a composition consistent with this stoichiometry, rather than a calcium-rich one that would reduce or suppress the co-precipitation of CH. At this point, it is important to emphasize that the solubility of CH is significantly higher than that of the C-S-H phases[16] and that the early C-S-H phase often has a variable composition with a higher calcium content[17], different from that specified in Eq. 1.

Until now, the reason for the inability to detect CH in the first hours of cement hydration has remained unresolved. The "silicate poisoning" theory

[1]Chair for the Chemistry of Construction Materials, Department of Chemistry, TUM School of Natural Sciences, Technical University of Munich, Garching bei München, Germany. [2]Chair for Surface and Interface Physics, Department of Physics, TUM School of Natural Sciences, Technical University of Munich, Garching bei München, Germany. [3]Jülich Centre for Neutron Science (JCNS) at Heinz Maier-Leibnitz Zentrum (MLZ), Forschungszentrum Jülich, Garching bei München, Germany. e-mail: torben.gaedt@tum.de

suggests that the dormant period of cement hydration is primarily influenced by delayed CH nucleation, caused by dissolved silicate species poisoning CH nuclei[18,19]. These mobile silicate species adsorb onto the active growth surfaces of embryonic CH nuclei, inhibiting nucleation and growth of portlandite[20]. During initial hydration, dissolved Ca^{2+} and OH^- ions thus accumulate until the poisoning effect is overcome, leading to rapid CH precipitation at the beginning of the acceleration period[7]. The CH forming in the early stages of cement hydration was also proposed to be incorporated into the initial C-S-H phases[21,22], to exist as small microcrystalline particles[23,24], or as an amorphous phase[25,26]. To date, no ultra-small CH particles with distinct crystalline shapes have been observed in cementitious samples during the initial stages, i.e., during the first few hours of cement hydration. This indicates that either the CH is dissolved in the pore solution that is metastable with respect to CH nucleation, or that the early CH phase is small in size and amorphous in nature.

A few reports from the late 1970s and early 1980s addressed the possible existence of an ACH (amorphous calcium hydroxide) phase during C_3S hydration. One line of evidence for such a phase is indirect, arising from discrepancies among analytical methods rather than from direct observation. Odler and Dörr found that the CH content of hydrating C_3S pastes measured by PXRD was systematically lower than that determined by thermogravimetry or solvent extraction, and concluded that part of the CH must therefore be present in an amorphous form[27]. In a companion study, seeding with crystalline CH failed to shorten the induction period of C_3S hydration, which the authors took as evidence against classical crystallization of CH from a supersaturated solution and led them to propose a two-step formation pathway involving an amorphous intermediate phase[28]. A similar discrepancy between PXRD and thermogravimetric or extraction methods was also reported by Midgley for set cement paste, alongside spherical ACH particles of approximately 100 nm observed by SEM amid the predominant crystalline CH platelets[29].

This direct morphological evidence for spherical nanoparticles on hydrating C_3S surfaces has also been reported by other authors, although their phase identity was assigned inconsistently across studies. Ings and coworkers observed spheres approximately 1 μm in size on C_3S single crystals after 30 min of hydration, which they attributed to amorphous or poorly crystallized CH and which were subsequently converted into acicular C-S-H after 60 min[30]. Ménétrier et al. observed morphologically similar but smaller particles on C_3S surfaces within a comparable time frame, but interpreted them as an early, poorly ordered form of C-S-H rather than CH[31]. More recently, Rheinheimer and Casanova used SEM and atomic force microscopy (AFM) to observe growing aggregated spherical nanoparticles on hydrating C_3S thin films, which they, however, attributed to C-S-H based on concurrent X-ray photoelectron spectroscopy (XPS) evidence of silicate polymerization[32,33]. Taken together, these studies consistently report that CH is undetectable as a crystalline phase during the earliest stages of C_3S hydration, coinciding with the appearance of spherical amorphous nanoparticles. Yet they disagree on whether these nanoparticles are CH or C-S-H and whether they represent a genuine amorphous precursor phase or a transient surface phenomenon.

Despite these earlier findings, the prevailing view in textbooks is that ACH does not exist during early cement hydration[8,34]. However, in recent years, the theory of "non-classical" nucleation pathways has brought the existence of ACH back into consideration[35]. Nowadays, portlandite is believed not to form classically but, like the C-S-H phases[36–38], in a multi-stage "non-classical" crystallization process akin to calcium carbonate ($CaCO_3$)[39,40]. Rodriguez-Navarro and coworkers and Madeja et al. have recently demonstrated the existence of ACH in model systems[41–43]. Their research has examined the "non-classical" crystallization of CH in (co-) titration experiments and demonstrated how polymer additives influence this complex multi-step process. Initially, complexes and clusters of ions form, which subsequently merge into amorphous nanoparticles. These particles then aggregate and create networks, eventually transforming into hexagonal portlandite crystals[42,43]. Functional polymers affect this "non-classical" crystallization pathway of portlandite by stabilizing the ACH phases, thus delaying crystallization[43]. They also modify the number, size, and morphology of the CH crystals formed[42]. Moreover, using in situ TEM measurements, Kang et al. showed that spherical ACH nanoparticles of approximately 100 nm in size are formed in solution when CaO is dissolved in water[44]. Recently, Guzmán García Lascurain et al. indeed discovered ACH nanoparticles in slaked lime, which were stabilized by microcellulose added before the lime slaking process. Microcellulose acts as a stabilizing template, preventing mineral crystallization and prolonging the liquid precursor phase of CH for up to 4 h. This stabilization enabled the successful isolation and ex situ analysis of ACH[45].

To clarify the native state of CH during the early stages of cement hydration, we studied the formation of this amorphous precursor phase from the pore solution of a technical Portland cement. We investigated isolated cementitious pore solutions using conventional and cryo-high-resolution transmission electron microscopy (cryo-HRTEM) combined with small-angle X-ray scattering (SAXS), pair distribution function (PDF) analysis, and macroscopic precipitation experiments. Our results demonstrate that rapid drying of the pore solution during conventional TEM sample preparation results in the formation of large (up to 1 μm) spherical ACH particles, which subsequently aggregate into hexagonal CH crystals with a morphology typical of Portland cement. In contrast, cryo-HRTEM combined with SAXS and PDF analysis of the native pore solution reveals the absence of these particles, showing instead only metastable gypsum prenucleation clusters of approximately 1 nm in diameter. This indicates that portlandite is completely dissolved in the pore solution during the early stages of cement hydration. Furthermore, we demonstrated that isolated pore solutions are highly metastable at room temperature under an inert atmosphere, a phenomenon attributable to the presence of different ions, particularly sulfates and silicates, which inhibit portlandite precipitation. Precipitation experiments conducted at elevated temperatures further confirm that, after prolonged induction times, only portlandite and gypsum precipitate from the separated pore solution, with no other hydrate phases, such as C-S-H or ettringite, forming. Our findings provide additional evidence that mineral phase nucleation is driven by distinct "non-classical" pathways, not only in controlled model systems and natural environments, but also in large-scale, multiphase materials such as Portland cement.

Results and discussion

The formation of ACH from separated cementitious pore solution

Portlandite is undetectable on the surface of hydrating cement particles during the first hour of cement hydration[12,15,46]. Consequently, it can be inferred that the initial formation of CH must occur within the aqueous phase. To analyze the composition of the aqueous phase during cement hydration, it is necessary to remove the solid constituents, such as the cement and the larger hydration products that predominantly nucleate on the surfaces of dissolving particles, by separating the pore solution. Several standard methods can be employed to separate the pore solution from a cement paste, including centrifugation, dead-end filtration, and continuous crossflow filtration[47–51]. Following separation, elemental analysis of the separated pore solution is typically performed using optical emission spectroscopy with inductively coupled plasma (ICP-OES)[49,51,52]. In our experiments, we mixed technical Portland cement with ultrapure water containing no additives. We then separated the pore solution from the cement paste after 15 min using dead-end filtration once the initial hydrate phase formation had subsided. We opted for dead-end filtration because, compared with the other separation methods mentioned, it enabled us to quickly obtain larger volumes of the pore solution in its original composition. Initially, we anticipated that the obtained clear pore solution would contain no nanoparticles after filtration, as nanostructured ettringite, nano-AFm, and nano-C-S-H particles typically nucleate on the surface of the dissolving cement particles and are only stabilized and dispersed in the pore solution in the presence of stabilizing additives such as dispersants[52]. However, contrary to our expectations, we observed ACH nanoparticles under the TEM after we applied the separated pore solution to a TEM grid at room temperature and allowed it to dry (see Fig. 1a–c and SI, Figs. S2–S4).

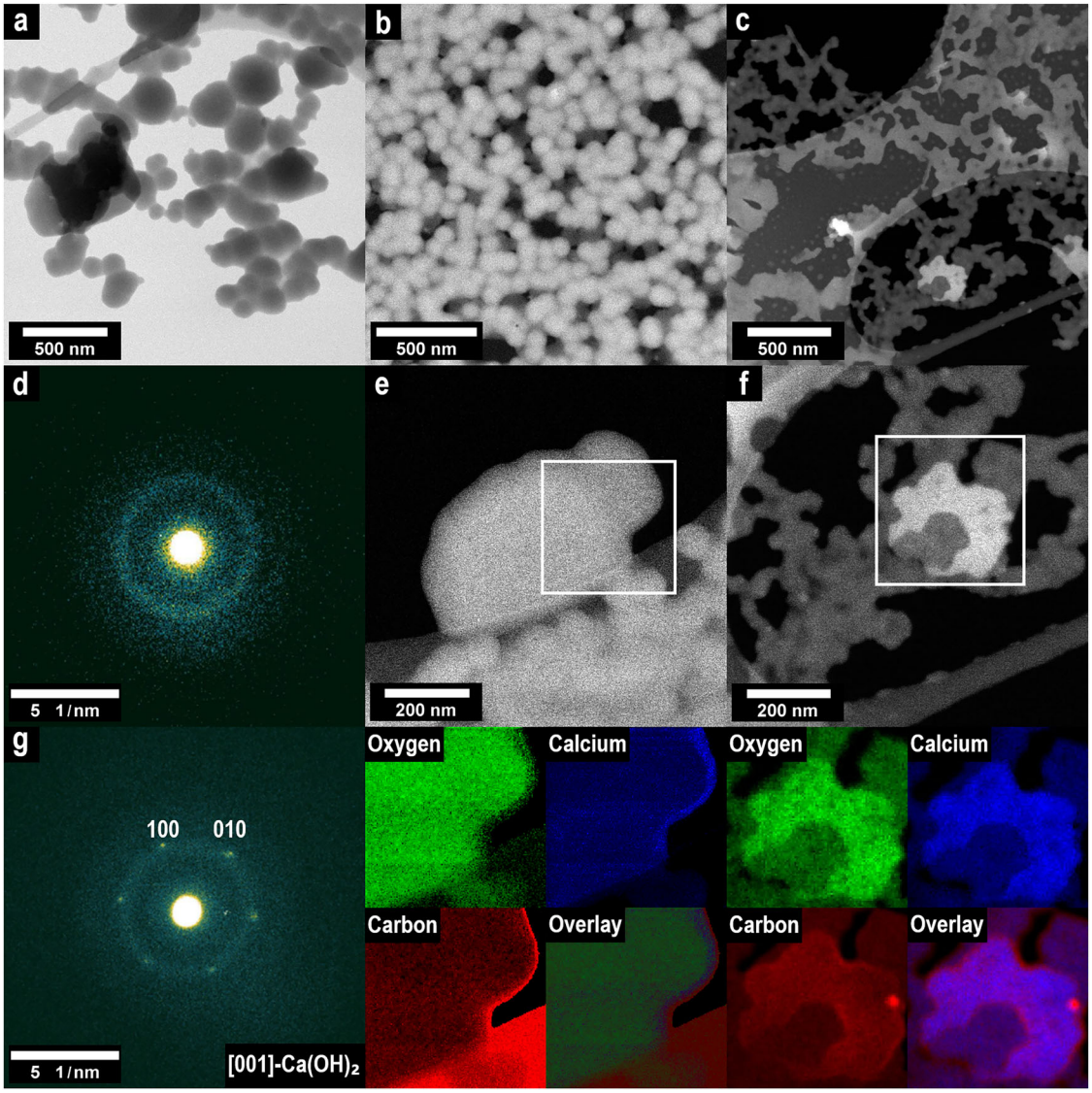


Fig. 1 | Electron micrographs of dried cementitious pore solution separated 15 min after the start of hydration, along with SAED and EELS measurements conducted in the highlighted areas. Bright-field scanning transmission electron microscopy (BF-STEM) image (**a**) and annular dark-field scanning transmission electron microscopy (ADF-STEM) images (**b**, **c**) measured with a low electron dose to protect the sample. Scale bars represent 500 nm. SAED patterns acquired at dose rates of 0.62 $e^-/Å^2/s$ (**d**) and 2.40 $e^-/Å^2/s$ (**g**), respectively. Upon exposure to the higher dose, the characteristic diffraction pattern of portlandite emerges (ICSD: 91882). Scale bars represent 5/nm. **e**, **f** EELS mapping in the highlighted areas reveals the core-shell structure and elemental composition of the particles. Scale bars represent 200 nm.

As will be demonstrated below, these particles do not represent the native state of CH in the pore solution but are instead formed as an intermediate phase during drying of the pore solution on the TEM grid.

The spherical nanoparticles detected using TEM have diameters between 100 and 200 nm (see SI, Fig. S3) and occur in agglomerates (see SI, Fig. S29). The elemental composition of the particles was analyzed using EELS (see Fig. 1e, f and SI, Figs. S28 and S30). The particles consist of calcium and oxygen and feature a core-shell structure. Given that the core exhibits low calcium but high oxygen signals, this is consistent with a core primarily composed of water. In contrast, the shell contains a higher concentration of calcium ions (see Fig. 1e). Because the sample was handled in the air, a carbon layer formed on the outermost edge of the particles (see Fig. 1f). During the short time while the pore solution dried on the TEM grid, the particle surfaces consequently reacted with atmospheric CO_2. A low-dose SAED pattern (dose 0.62 $e^-/Å^2/s$) showed only a diffuse halo, revealing the amorphous nature of the particles (see Fig. 1d). When exposed to the electron beam at a higher dose rate (2.40 $e^-/Å^2/s$) for a short time, the particles rapidly crystallize into portlandite, as evidenced by the appearance of characteristic SAED reflections of crystalline CH (see Fig. 1g). This beam-induced crystallization reflects the high sensitivity of the hydrated amorphous particles to higher dose rates. Under intense irradiation, the amorphous particles undergo structural changes due to radiolysis[42]. Notably, the portlandite reflections emerge within the diffuse halo of the original amorphous phase, indicating that both phases share identical d-spacings. This strongly supports the conclusion that the amorphous precursor is structurally related to portlandite. Moreover, these observations provide additional nanoscale structural evidence for the non-crystalline intermediate phase of CH, first reported by Rodriguez-Navarro and coworkers[41,42].

We further examined the ACH particles using SEM. During SEM examination, we observed a continuous network of approximately 1 µm spheres (see Fig. 2a and SI, Fig. S31), alongside small scattered ACH particles (see SI, Fig. S32) and their larger aggregates identified previously under the TEM (see SI, Fig. S33). These particles were uniformly shaped, similar in

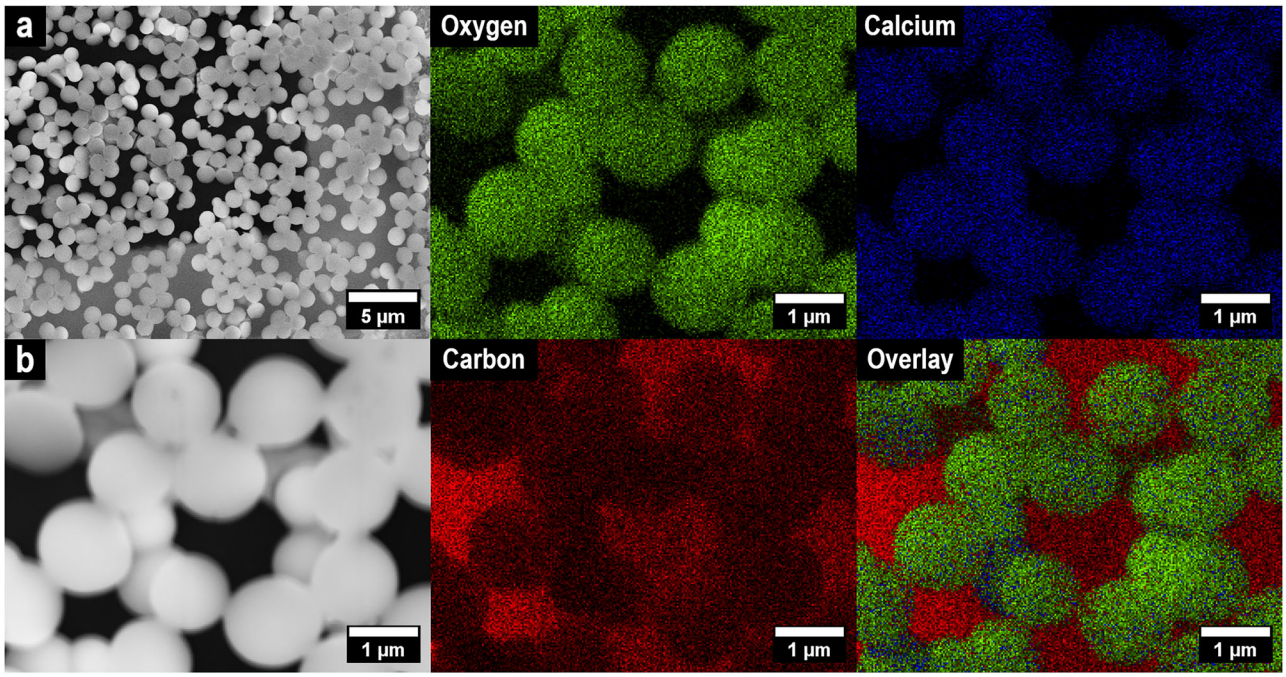


Fig. 2 | SEM-EDX data of ACH particles observed after depositing a cementitious pore solution, separated 15 min after the start of hydration, onto a TEM grid. **a** SEM micrographs of a contiguous network of uniformly shaped 1 µm spheres interconnected at their edges. Scale bar represents 5 µm. **b** SEM-EDX maps of the area revealed the elemental composition of the particles. Scale bars represent 1 µm.

size, and interconnected at their edges. Notably, they began to deform at their edges due to water loss during exposure to the electron beam. Some aggregates were even embedded in a layer of dried potassium sulfate (see SI, Fig. S34). The elemental composition of the spherical particles was determined through energy dispersive X-ray (EDX) measurements (see Fig. 2b and SI, Figs. S35–S38). The particles primarily consist of oxygen and calcium, as well as a small amount of carbon, resulting from unavoidable surface carbonation in accordance with TEM results, confirming that the observed particles are indeed ACH particles. Other detected elements (see SI, Tables S2 and S3) originate from the surface (TEM grid, silicon wafer) on which the sample was applied (copper, silicon), or from dissolved sulfate species in the pore solution (potassium, sodium, and sulfur).

Impact of sample preparation on the appearance of the ACH nanoparticles

ACH from cementitious and model supersaturated CH solutions. We first examined whether the technique used to separate the cementitious pore solution or the *w/c* ratio used in mixing the cement affected the observations under the TEM. We detected spherical ACH nanoparticles from all cementitious pore solutions that we isolated and dried. Neither the separation method (see Fig. 3a, b and SI, Figs. S5–S8) of the pore solution nor the selected *w/c* ratio (see Fig. 3c and SI, Figs. S9 and S10) noticeably affected the appearance of the ACH nanoparticles in the TEM micrographs. Experiments conducted at $w/c = 0.5$ and $w/c = 0.75$ (see Fig. 3c) yielded ACH particles that were morphologically identical to those observed at $w/c = 1.0$ (see SI, Figs. S9 and S10), confirming that the appearance, morphology, and formation mechanism of ACH are insensitive to the *w/c* ratio within this range. To determine whether the ACH nanoparticles are a characteristic feature of a cementitious system or can be obtained from any supersaturated CH system, we also conducted various model experiments designed to create supersaturated CH solutions. Additional information regarding these experiments can be found in the Supplementary Information. Amorphous spherical nanoparticles were found in supersaturated CH solutions obtained by dissolving calcium oxide (CaO) or calcium metal (Ca) in water (see Fig. 3d, e and SI, Figs. S11 and S12), by combining a calcium chloride ($CaCl_2$) solution with a sodium hydroxide (NaOH) solution (see SI, Fig. S13), or by separating the pore solution of mixed slaked lime or C_3S (see Fig. 3f and SI, Fig. S14). Consequently, whenever a supersaturated CH solution is dried on a TEM grid, spherical amorphous nanoparticles form.

However, the nanoparticles observed in electron micrographs of the cementitious pore solution varied in size. While the majority of the particles ranged between 100 and 200 nm (see SI, Fig. S3), we also found significantly larger particles measuring up to 1 µm (see SI, Fig. S3), as the hydrated amorphous particles tend to agglomerate strongly. The larger particles must have formed during the slow drying process on the TEM grid after the separation rather than in solution, since they could not have passed through the filter (0.45 µm). Importantly, ACH particles could even be observed when an undersaturated CH solution (0.01 M) was applied to a TEM grid (see SI, Fig. S15), probably because the solution becomes supersaturated while drying on the grid.

TEM preparation methods. We also observed noticeable differences in the appearance of the ACH nanoparticles when the TEM grid was prepared using different methods. Four different standard preparation protocols were tested (see SI, Fig. S1): (1) drop-casting, (2) blotting, (3) quenching with ethanol as described by Rodriguez-Navarro and coworkers[42], and (4) cryo-TEM preparation. The preparation method significantly influenced the shape, size, and agglomeration degree of the observed ACH nanoparticles (see Fig. 4). This is consistent with the well-documented behavior of two other inorganic systems that likewise do not crystallize classically—gypsum ($CaSO_4{\cdot}2H_2O$)[53,54] and calcium carbonate ($CaCO_3$)[39,40]—for which slow drying and chemical quenching (such as with ethanol) have been shown to introduce severe artifacts and to strongly influence crystallization kinetics of these materials, thereby obscuring the native state of the crystallizing solution[55].

Effect of TEM preparation–blotting. When the samples were prepared by blotting the cementitious pore solution onto a TEM grid, the grid became covered with numerous round ACH particles (see Fig. 4a and SI, Fig. S16). Since the drying rate depends on several factors, such as humidity, temperature, and atmosphere—none of which were

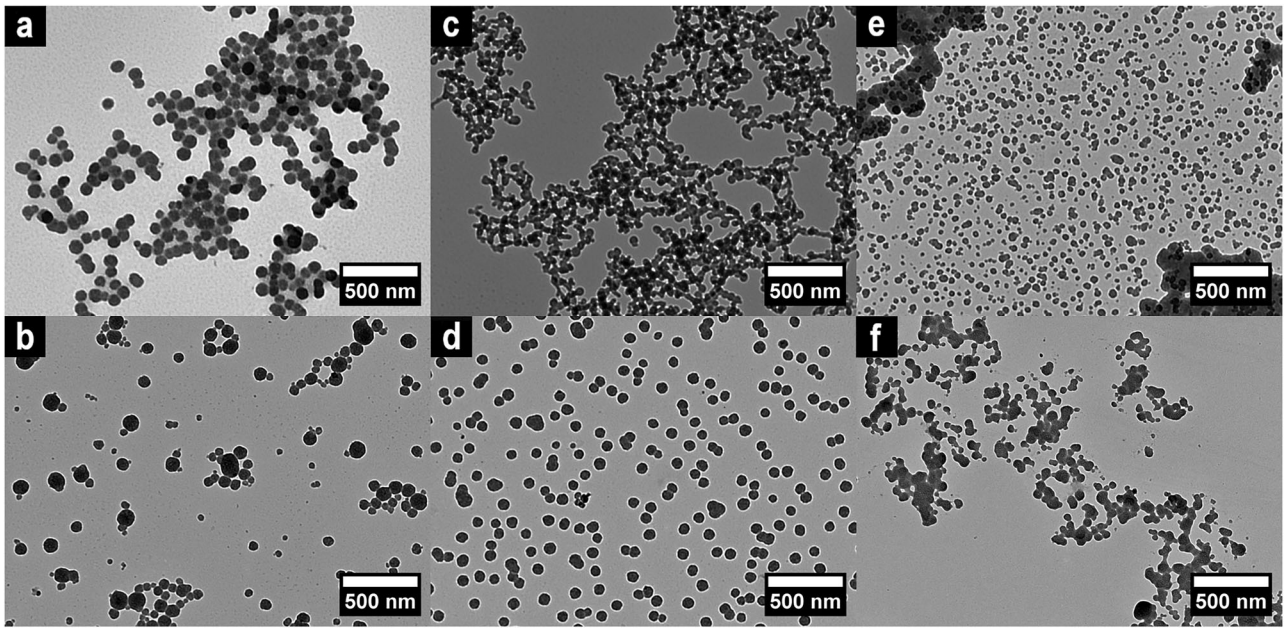


Fig. 3 | Electron micrographs of ACH nanoparticles formed during drying of different supersaturated CH solutions on a TEM grid. Cementitious pore solutions separated by centrifugation at $w/c = 1.00$ (**a**), continuous cross-flow filtration at $w/c = 1.00$ (**b**), and dead-end filtration at $w/c = 0.75$ (**c**). Model supersaturated CH solutions were obtained by dissolving calcium oxide (**d**) or calcium metal (**e**) in water. **f** C_3S pore solutions separated by dead-end filtration at $w/c = 1.00$. All TEM samples were prepared identically using the blotting method. Scale bars represent 500 nm.

controlled, except that all samples were prepared at room temperature—the spheres can grow to different sizes and agglomerate to varying degrees. In some extreme cases, this even led to the formation of a densely packed percolated network of particle aggregates on the TEM grid (see SI, Fig. S17). The different observations across samples are thus attributable to uncontrolled blotting parameters that led to a significant variability in the drying rate and are consistent with a formation mechanism involving a dense liquid phase via liquid-liquid phase separation during the drying process. Conducting a mechanistic study with a standardized drying protocol in a humidity-controlled chamber would be of particular interest, as it would allow systematic adjustment of the drying rate to clarify the exact mechanism behind ACH formation.

Nonetheless, we observed distinct stages that the ACH undergoes on its path to crystalline CH, which occurred simultaneously within the same sample (see SI, Figs. S9 and S10). Despite our best efforts to maintain consistent hydration and preparation conditions, ACH appeared in various shapes across samples prepared using identical protocols. We postulate that differences in the drying rate, caused by local variations in the thickness of the liquid film layer, preserved ACH at distinct stages of its transformation into crystalline CH, allowing us to observe the progression of CH crystallization (see Fig. 5). The ACH nanoparticles (see Fig. 5a) can aggregate into much more complex agglomerate structures comprising particles of different sizes (see Fig. 5b and SI, Fig. S22). As the primary particles forming the agglomerates became less spherical, increasingly condensed and coalesced aggregates were formed (see Fig. 5c and SI, Figs. S23 and S24). Ultimately, in addition to the spherical ACH nanoparticles, contiguous structures emerge (see Fig. 5d, e and SI, Figs. S25 and S26), which grow together and gradually adopt the characteristic hexagonal shape of CH crystals that would form later (see Fig. 5f). In conclusion, the ACH transforms into crystalline CH when the residual water evaporates from a thin film of the cementitious pore solution deposited on a TEM grid. The aggregation of spherical particles into hexagonal shapes, characteristic of CH formed in cementitious systems, indicates that this process can be classified as a "non-classical" crystallization (see Fig. 5g). The mechanism of CH crystallization from cementitious pore solutions is thus consistent with predictions made in previous studies involving model systems by Rodriguez-Navarro and coworkers and Madeja et al.[42,43].

While we cannot provide direct in situ evidence for ACH formation within the constrained, water-saturated pores of hydrating cement paste, some findings suggest that the "non-classical" crystallization pathway discussed here is also relevant to real cement systems. First, it is important to note that although the pore solution contains many foreign ions at high concentrations, the CH crystallization process appears to proceed similarly to that observed in pure model systems without additional ions[42,43]. Moreover, the spherical particles observed on the surfaces of hydrating C_3S and OPC in various SEM studies[29–33] are most plausibly reinterpreted as ACH formed during sample preparation, rather than as native surface species. Furthermore, portlandite is known to form preferentially within capillary pores and cavities in hardening cement paste[25,56–58], rather than uniformly on the surfaces of cement particles, as other hydrate phases do[59]. This preferential location and the resulting non-uniform, clustered distribution of crystalline portlandite in hardened cement paste suggest that a transient ACH stage forming at these interfaces may facilitate portlandite crystallization in these regions. However, we emphasize that confirming this mechanism in cement paste will require future investigations using advanced in situ scattering and microscopy techniques, which are beyond the scope of this study.

Effect of TEM preparation–drop casting. An entirely different picture emerged when the cementitious pore solution was drop-casted onto a TEM grid. The TEM grid appeared to be almost empty under the electron microscope. Only at high magnifications, tiny particles (less than 20 nm) could be detected, though many of these particles were already highly agglomerated (see Fig. 4b and SI, Fig. S18). In contrast to the blotting method, the significantly faster drying process does not allow the ACH particles sufficient time to grow to sizes of 100 nm. This indicates that the ACH particles in solution must be very small, perhaps even within the size range expected for prenucleation clusters (less than a few nanometers)[60]. Hence, the TEM sample preparation method governs the observations in TEM micrographs rather than the intrinsic properties of the nanoparticles or the characteristics of the pore solution.

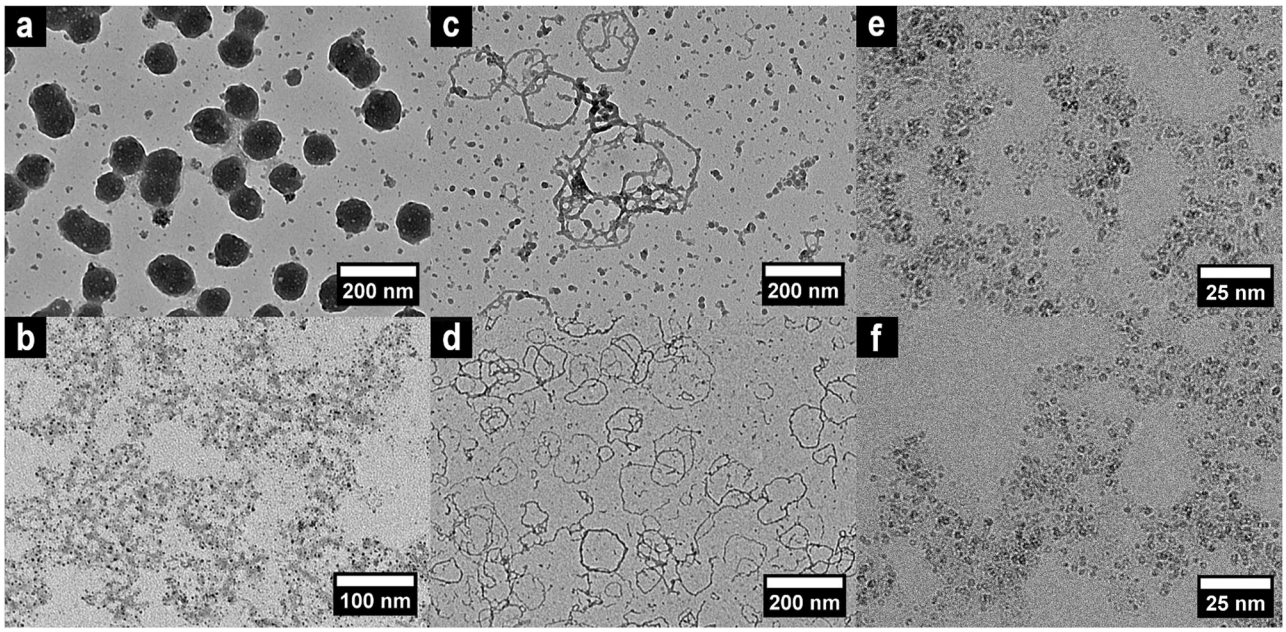


Fig. 4 | Electron micrographs of ACH nanoparticles observed on differently prepared TEM grids. a Spherical particles measuring approximately 100 nm were found using the blotting method. Scale bar represents 200 nm. **b** Significantly smaller agglomerated particles were observed by the drop-casting method. Scale bar represents 100 nm. **c** Ring-like hexagonal agglomerates composed of primary spherical particles produced by quenching a C_3S pore solution with ethanol (1:10). Scale bar represents 200 nm. **d** For comparison, an undersaturated CH solution (0.01 M) quenched with ethanol. Scale bar represents 200 nm. **e**, **f** Cryo-TEM images of separated cementitious pore solution measured with a cryo-TEM. Scale bars represent 50 nm.

Effect of TEM preparation–ethanol quenching. The quenching with ethanol before blotting has been reported to minimize artifacts during sample preparation and provide TEM images with nanostructural features of metastable precursor phases similar to those observed in cryo-TEM[42]. However, for the technical cement, this protocol caused the precipitation of various potassium and calcium sulfates, such as arcanite (K_2SO_4) or syngenite ($K_2Ca(SO_4)_2 \cdot H_2O$), from the cementitious pore solution. The TGA-MS measurements of the isolated precipitate (see SI, Fig. S52), revealed, besides the water loss of syngenite, a second weight loss event at 410 °C, which is shifted by 50 °C compared to the calcination stage of portlandite (460 °C)[47]. Additionally, the FTIR spectrum of the dried precipitate displayed a distinct peak corresponding to hydroxide vibrations around 3600 cm^{-1}, alongside the expected vibrational modes of arcanite and syngenite (see SI, Fig. S68). Notably, the powder X-ray diffractogram of the precipitate showed, in addition to the reflexes of arcanite and syngenite, very broad reflexes at the positions where the reflexes of portlandite are expected (see SI, Fig. S60). These results indicate that quenching cementitious pore solutions with ethanol preserves portlandite in an amorphous or at least partially crystalline state.

To prevent the formation of an undesired precipitate, we repeated the ethanol-quenching experiment using a pore solution of the pure phase C_3S instead of technical cement. After quenching with ethanol, no precipitate formed since no sulfates are dissolved in the C_3S pore solution, which allowed us to prepare the TEM grid by blotting. Interestingly, the TEM images revealed not only individual spherical ACH nanoparticles but also ring-like hexagonal agglomerates composed of primary spherical particles, although it remained unclear whether these structures were in the process of formation or dissolution (see Fig. 4c and SI, Fig. S19). Comparable structures were also observed in TEM images of undersaturated CH solutions (0.1 M) that were similarly quenched with ethanol (see Fig. 4d and SI, Fig. S20). Rodriguez-Navarro and coworkers previously found similar structures[42]. However, their results could not be replicated in the cryo-TEM study conducted by Madeja et al.[43]. This discrepancy led Madeja et al. to assume that quenching with ethanol might play a significant role in the formation of these unique hollow structures. Adding ethanol changes the dielectric constant and activity of water[55], which in turn affects the solubility and drying rate of the pore solution. In the case of portlandite, this alteration presumably induces the formation of ring-like hexagonal structures that are not obtained when examining a pure pore solution. Notably, these results demonstrate that standard solvent-exchange protocols significantly alter the solvation environment, resulting in the formation of ring-like artifacts. This suggests that structures previously identified as native precursors in the literature may, in fact, be solvent-induced precipitates, highlighting the importance of in-situ techniques and cryo-TEM for characterizing crystallizing phases[55].

Cryo-TEM imaging of the pore solution. Due to the uncertainties associated with standard sample preparation methods, Ilett et al. proposed using cryo-TEM techniques as the most reliable approach for studying the earliest stages of crystallization. Although cryo-TEM methods cannot be wholly artifact-free, they arguably provide the most accurate representation of the native state of the particles in solution[55]. Consequently, we used cryo-TEM to determine the actual shape of the ACH nanoparticles in the pore solution. In the vitrified solution, significantly smaller particles (5–10 nm) could be found, although these particles were already highly agglomerated (see Fig. 4e, f and SI, Fig. S21). These findings were similar to those obtained in our experiments in which the TEM grid was prepared by the drop-casting method (see Fig. 4b and SI, Fig. S18). Accordingly, the considerably larger particles (100–200 nm) observed under the conventional TEM after drying (see Fig. 1 and SI, Fig. S3) only grow to their size during the drying process on the TEM grid and do not represent the native state of the particles in solution.

Cryo-HRTEM imaging of the pore solution. To minimize the formation of drying artifacts during vitrification and to preserve the native state of the pore solution to the greatest extent, we ensured that the contact time of the solution with the filter paper during blotting while vitrifying additional samples was kept as short as possible. We subsequently examined the samples prepared in this manner using a high-resolution cryo-TEM. This time, imaging was performed exclusively in areas of vitreous ice within the holes of the lacey carbon film—regions that were

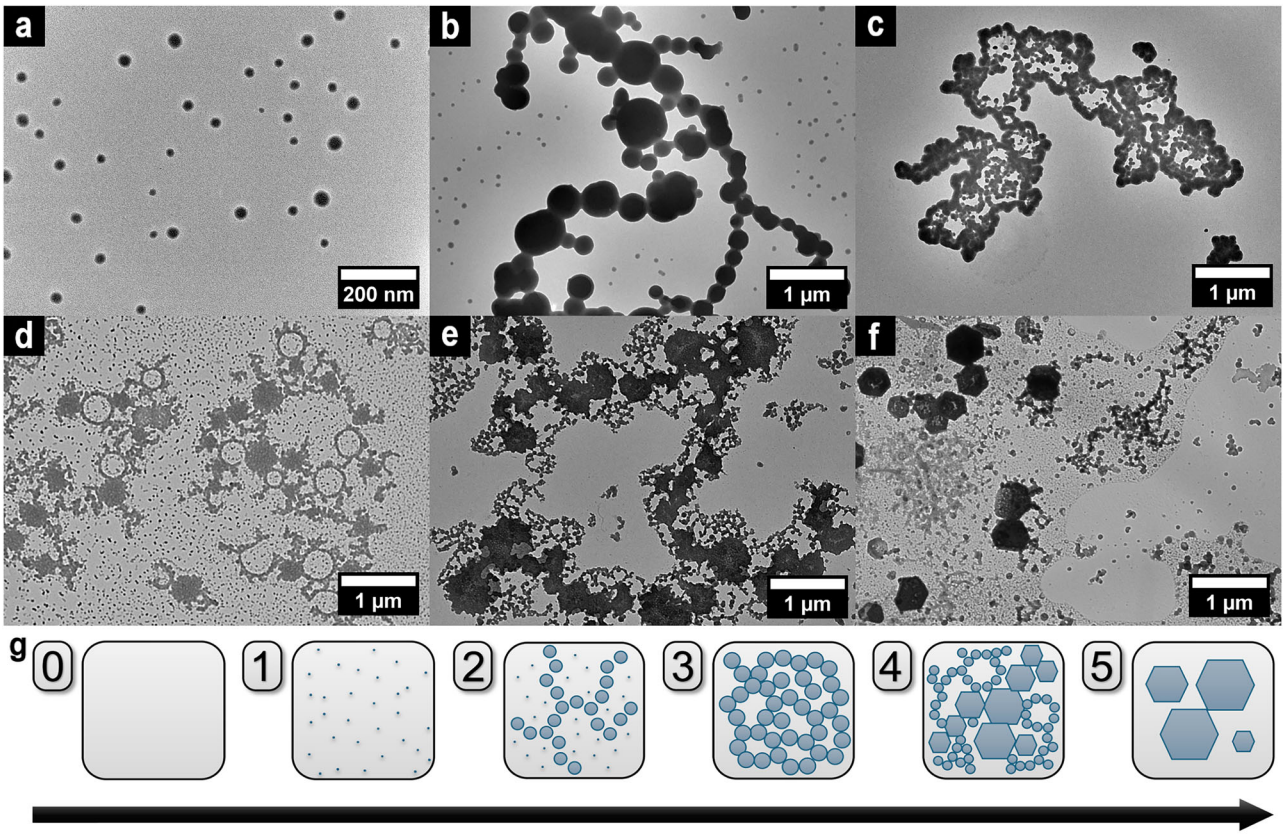


Fig. 5 | Multi-stage "non-classical" crystallization process of CH during drying on a TEM-grid. a–f Electron micrographs of dried cementitious pore solution separated 15 min after the start of hydration, prepared by the blotting method. The TEM images show ACH particles and aggregates at different stages of their morphological transformation during drying on the TEM grid, ranging from isolated amorphous spherical nanoparticles (**a**) through increasingly condensed aggregates (**b**–**e**) to crystalline structures adopting a hexagonal morphology (**f**). Scale bars represent 200 nm and 1 µm, respectively. **g** Schematic illustration of the proposed multi-stage "non-classical" crystallization pathway of CH, from dissolved ions (**0**) through ion complexes and clusters (**1**), amorphous spherical nanoparticles (**2**), nanoparticle aggregates (**3**), and percolated networks (**4**) to hexagonal portlandite crystals (**5**).

not in contact with the filter paper during blotting and therefore remained continuously submerged in an aqueous layer throughout sample preparation. Under these conditions, no ACH particles were detected. Instead, only small clusters with apparent sizes of 1–2 nm were observed (see Fig. 6b, c). Fast Fourier Transform (FFT) patterns of the corresponding HRTEM images revealed the presence of a calcium sulfate phase (insets in Fig. 6b, c). Notably, HRTEM images acquired at lower magnification (×250,000) and, correspondingly, a lower electron dose rate per recorded area revealed the presence of structurally ill-defined, weakly ordered clusters with sizes below 1 nm (see Fig. 6a). These clusters exhibited no clear lattice fringes, indicating a predominantly amorphous nature. This suggests that, upon imaging at higher magnification (×380,000) and increased dose rates, these sub-nanometer clusters underwent electron-beam-induced crystallization, resulting in the formation of crystalline calcium sulfate nanoparticles. These particles can be classified as prenucleation clusters, which have previously been reported for calcium sulfate[54,61].

This finding leads to the following conclusions: both CH and calcium sulfate form from cementitious pore solutions via "non-classical" crystallization pathways. Although both phases are nominally supersaturated in the pore solution during the first hour of cement hydration (see SI, Table S4), only prenucleation clusters of calcium sulfate were found, suggesting that the "non-classical" crystallization pathways for these two minerals are fundamentally different[62]. While calcium sulfate forms small prenucleation clusters in solution, no CH precursor species were detected above the detection limit of cryo-HRTEM (~1 nm). These results are most consistent with CH being present exclusively as fully solvated ions or ion pairs. However, it is important to note that this conclusion is based solely on the non-detection of CH-containing species and therefore represents a strong inference rather than definitive proof of their absence. The absence of ACH in the cryo-HRTEM measurements contrasts with the findings of Madeja et al., who detected ACH in cryo-TEM images[43]. This discrepancy can be rationalized by several key differences between the two studies. First, Madeja et al. employed standard cryo-preparation involving normal blotting, in contrast to our cryo-HRTEM preparation method, where we aimed to minimize blotting intensity. Second, their samples were drawn from pure model systems ($CaCl_2$ + NaOH), whereas the cementitious pore solution contains significant concentrations of other ions (see SI, Table S4), which can kinetically inhibit CH nucleation. Third, the degree of supersaturation with respect to CH in their model systems at the time of sampling (SI = 1.20–1.90) exceeded that of the cementitious pore solution after 15 min (SI = 0.55). Furthermore, the absence of large ACH particles in the vitrified pore solution is fully consistent with the SAXS and PDF analyses performed directly on the native liquid pore solution (see below), both of which confirm the presence of only sub-nanometer calcium sulfate species and thus validate the cryo-HRTEM findings.

SAXS and PDF study of the solution. To avoid any preparation artifacts, which might compromise the natural state of the cementitious pore solution, we performed a comprehensive analysis using small-angle X-ray scattering (SAXS) and pair distribution function (PDF) analysis techniques. To ensure relevance to real conditions, SAXS and PDF analysis were conducted directly on the separated cementitious pore solution in its native liquid state, enabling structural characterization

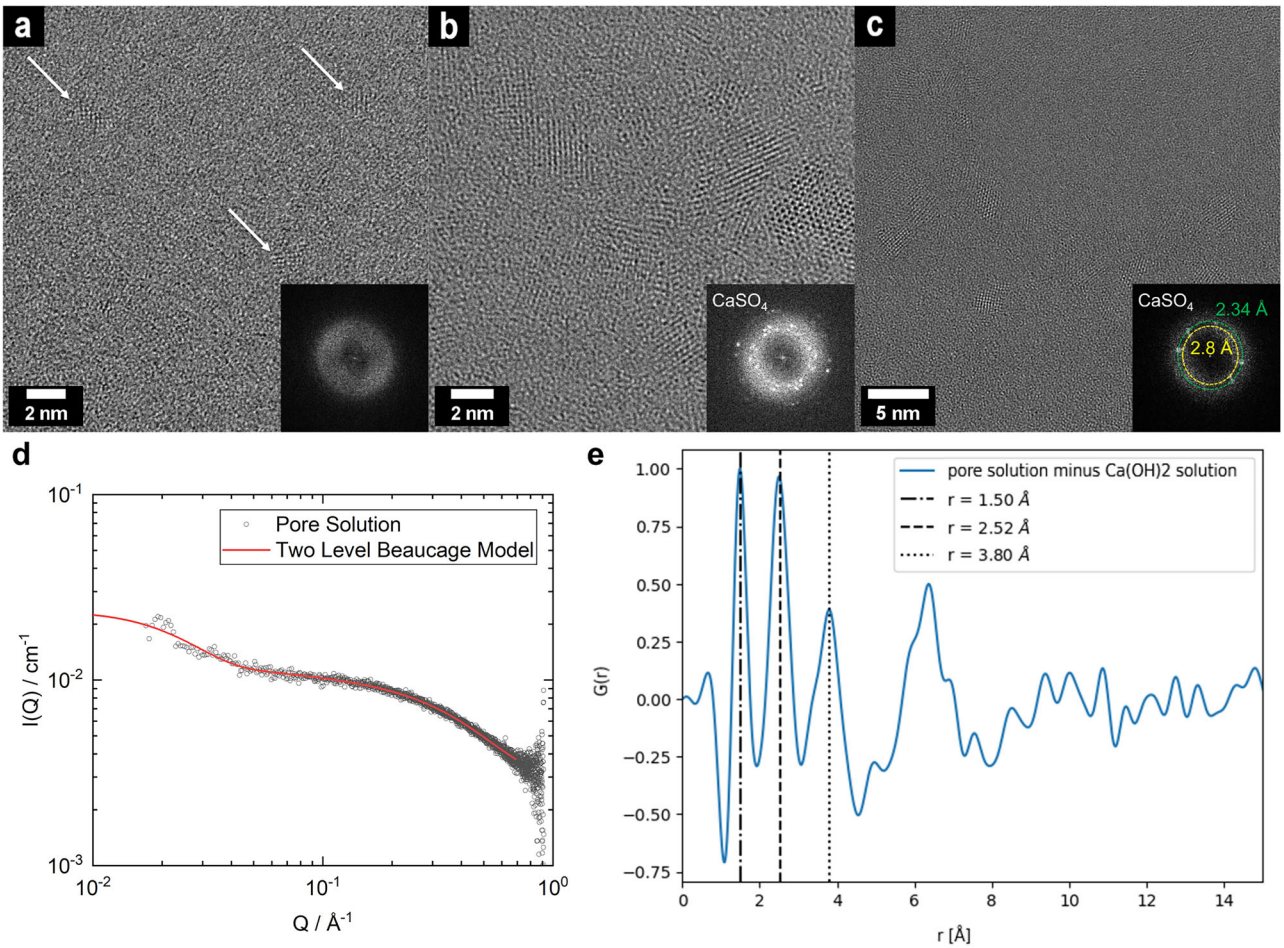


Fig. 6 | Structural characterization of separated cementitious pore solution. **a**–**c** High resolution transmission electron micrographs of vitrified cementitious pore solution separated 15 min after the start of hydration. The observed amorphous sub-nanometer clusters (**a**) crystallize into tiny nanoparticles (1–2 nm) induced by the electron beam at higher dose rates (**b**, **c**). Scale bars represent 2 nm (**a**, **b**) and 5 nm (**c**), respectively. **d** The SAXS profile of the cementitious pore solution with a two-level Beaucage model[64]. **e** PDF analysis from cementitious pore solution minus an undersaturated (0.01 M) CH solution.

without drying artifacts. SAXS is a well-established method in materials science for characterizing particulate systems, such as colloidal suspensions[63]. We employed SAXS to characterize the size and morphology of primary particles and agglomerated species present in the cementitious pore solution. The SAXS profile with a two-level Beaucage model[64] (see Fig. 6d) reveals the presence of nearly spherical primary particles exhibiting a gyration radius (R_g) of approximately 0.37 nm (equating to ~1 nm in diameter for a spherical entity) in addition to corresponding clusters with a gyration radius of roughly 7 nm. Applying the Schutzsphere model[65] for spherical particles produced a narrow diameter distribution and an excellent fit for the scattering behavior of the primary particles (see SI, Fig. S77), with an average diameter of 1.06 nm (see SI, Fig. S78). This SAXS-derived size provides a preparation-artifact-free quantitative measure of the native particle size, in direct contrast to the size distributions obtained from dried TEM samples (see SI, Figs. S2–S4). The results of the SAXS measurements thus confirmed that the large ACH spheres identified by electron microscopy do not accurately represent the native state of CH in the cementitious pore solution. Instead, these findings suggest the existence of tiny prenucleation clusters in the pore solution with diameters of approximately only 1 nm.

To characterize the local atomic structure of the amorphous phase present in the cementitious pore solution, we performed differential PDF analysis using high-energy X-ray scattering data collected at the European Synchrotron Radiation Facility (ESRF). An undersaturated CH solution (0.01 M) served as a reference to isolate structural features specific to other phases. The resulting differential PDF (see Fig. 6e) exhibits distinct peaks at 1.50, 2.52, and 3.80 Å, corresponding to the S-O, Ca-O and Ca-Ca/S-S interatomic distances, which are characteristic of calcium sulfate pre-nucleation clusters[66]. These characteristic distances and the fingerprint of the abstracted differential PDF closely resemble those reported for calcium sulfate prenucleation clusters in the study by Stawski et al. on the formation pathway of gypsum ($CaSO_4{\cdot}2H_2O$) from aqueous solution. Using molecular dynamics simulations, the authors derived the structures of small calcium sulfate clusters that serve as precursors for crystalline gypsum. The strong agreement between our experimentally derived differential PDF and the MD-validated PDF signatures presented by Stawski et al. suggests that the amorphous phase detected in the cementitious pore solution can be attributed to similar calcium sulfate precursor clusters[66]. Additionally, the absence of long-range order, indicated by the termination of PDF oscillations between 8 and 10 Å, indicates a coherent structural correlation length of less than 1 nm, which is consistent with the amorphous, ultra-small domains detected by SAXS (see Fig. 6d) and cryo-HRTEM (see Fig. 6a–c).

Overall, these results provide conclusive evidence for the existence of amorphous calcium sulfate prenucleation clusters in the cementitious pore solution after 15 min of hydration. Similar to cryo-HRTEM, no CH precursors were detected in the PDF analysis (see SI, Fig. S79), despite the solution being supersaturated with respect to both calcium sulfate and CH (see SI, Table S4). This strongly suggests that the ACH nanoparticles observed in conventional TEM arise during sample drying and do not reflect the true state of CH within the cementitious pore solution. To accurately

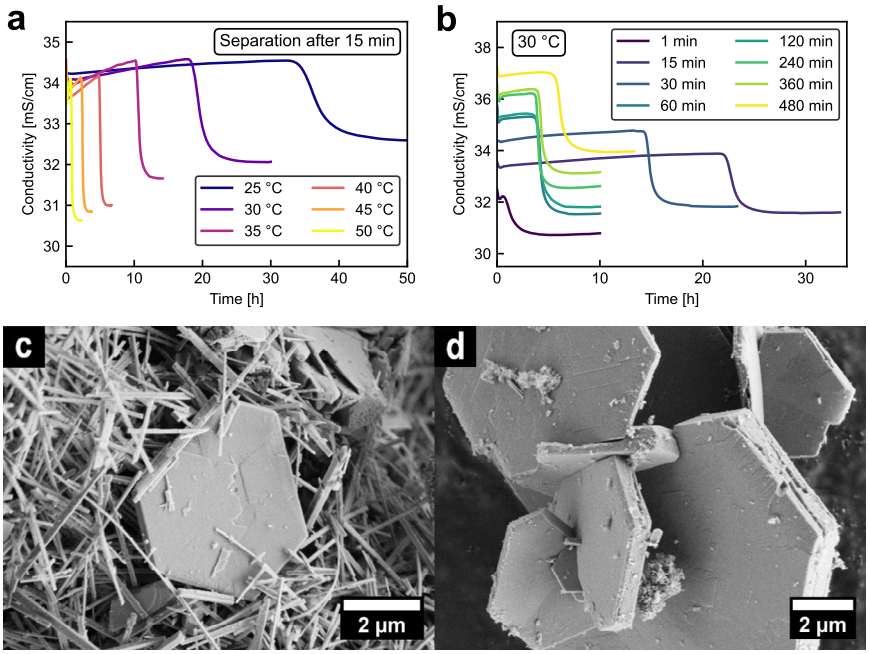


Fig. 7 | Dependence of the induction time for CH precipitation from cementitious pore solution on the temperature and the separation timing of the pore solution. a Conductivity measured over time at different temperatures of cementitious pore solutions separated 15 min after the start of hydration. **b** Conductivity measured over time at 30 °C of cementitious pore solutions separated at different times after the cement hydration started. The determined induction times are provided in the SI, Section S5. SEM images of the isolated precipitates, when separation took place after 15 min (**c**), and after 1 h (**d**). Scale bars represent 2 µm.

elucidate this state and the pathways of CH nucleation and growth in solution, it is imperative to conduct further investigations of cementitious pore solutions employing advanced high-resolution in situ scattering techniques, in combination with atomistic simulation methods, such as molecular dynamics (MD) simulations[62], which, however, exceed the current scope of the present study. It should also be noted that the structural characterization was performed exclusively on cementitious pore solution separated after 15 min of hydration, which represents the early dormant period of cement hydration. Whether CH prenucleation clusters or ACH may form at later stages of the induction period cannot be excluded or confirmed based on the present data and represents an important direction for future investigations.

Precipitation of calcium hydroxide and gypsum from separated cementitious pore solutions

In conjunction with the electron-microscopic analysis of the separated cementitious pore solution and the ACH intermediate phase formed during drying the pore solution on a surface, we conducted a comprehensive series of macroscopic precipitation experiments using the separated pore solutions. By identifying the precipitating species after a defined induction time and determining the effects of various parameters, such as temperature, the timing of pore solution separation, and pore solution sulfate concentration, we aimed to enhance our understanding of CH precipitation in cement pastes. A separated cementitious pore solution remains stable for several days when stored under an inert gas atmosphere at low temperatures. Under these conditions, no precipitate forms from the solution, and even after several days, amorphous spherical nanoparticles can be observed using conventional TEM, in full analogy to the experiments described above. However, in precipitation experiments conducted at elevated temperatures (25–50 °C), CH will homogeneously crystallize from the pore solution after an induction time, as demonstrated by thermogravimetric analysis-mass spectrometry (TGA-MS), powder X-ray diffraction (PXRD), and Fourier-transform infrared (FTIR) measurements (see SI, Sections S6–S8). The induction time, determined through conductivity measurements (see Fig. 7a and SI, Section S5), is temperature-dependent and decreases considerably with increasing temperature (see SI, Table S6 and Fig. S49). The onset of CH precipitation is accompanied by a significant decrease in conductivity, while the conductivity does not fall during the preceding induction period. As a result, the cementitious pore solution is considered metastable, with the formation of portlandite kinetically hindered under the conditions investigated.

Notably, the induction times for CH precipitation, measured at 30 °C, are also affected by the separation timing of the pore solution (see Fig. 7b and SI, Table S7 and Fig. S50). If the pore solution was separated from the cement paste immediately after mixing, gypsum precipitated within a few minutes (see Table 1 and SI, Figs. S39, S53, S61, and S69), as the aqueous phase is still supersaturated with respect to gypsum (SI, Table S4). At later separation times (15 min or 30 min), gypsum and CH co-crystallized from the pore solution at 25 °C, with the amount of gypsum decreasing over time (see Table 1, Fig. 7c and SI, Figs. S40, S54, S62, and S70). Conversely, if the pore solution was separated later, such as after 1 h or at higher temperatures (30 °C or more), only CH, not gypsum, precipitated after a specific induction period (see Table 1, Fig. 7d and SI, Figs. S41, S55, S63, and S71). For pore solutions separated after 1 or 2 h, during the dormant period of cement hydration (see SI, Fig. S76), the induction time for CH nucleation was more than halved at the same temperature compared to separation after 15 min (see SI, Table S7 and Fig. S50). The induction time further decreased slightly when the pore solution was separated after 4 or 6 h, during the acceleration period of cement hydration (see SI, Fig. S76). It is important to note that portlandite must have already formed within the cement paste by this stage, as its initial formation typically coincides with the start of the acceleration period[12]. Despite this, the pore solution remains supersaturated with respect to CH (see SI, Table S4)[28], allowing CH to precipitate from the solution after a specific induction period. The induction time then increased again if the pore solution was separated after 8 h. Beyond this point, further separation of the pore solution was no longer feasible, as the cement paste had solidified to such an extent that it could no longer be stirred.

The induction time of CH precipitation from separated pore solution, therefore, depends not only on the temperature but also on the chemical composition of the pore solution (see SI, Table S4). Since the soluble sulfate sources become depleted as the hydration of OPC progresses (see SI, Fig. S76), the sulfate concentration in the pore solution declines sharply in the first hour of cement hydration (see SI, Fig. S47). In particular, the initial rapid decrease in both sulfate and Ca^{2+} concentrations during the first 15 min is primarily attributable to ettringite formation[51]. This may indicate that CH precipitation is inhibited by sulfate ions in cementitious pore

solutions, which become increasingly reduced during the dormant period of cement hydration, thereby allowing CH to crystallize. Gypsum and alumina have a non-negligible kinetic influence on the nucleation of CH in cement paste, while the impact of alkali ions is minimal[56]. It is also plausible that the detected prenucleation clusters of gypsum in the pore solution (see Fig. 6) may interact with portlandite and subsequently serve as heterogeneous nucleation sites. In cement paste, the local environment around dissolving gypsum particles also promotes CH nucleation[56]. Interestingly, the induction time for CH precipitation from a pure C_3S pore solution, which was separated and tested under the same conditions, is found to be several times shorter than that from a cementitious pore solution: 8 h vs. 37 h at 25 °C (see SI, Table S8 and Fig. S51). However, if a small amount of gypsum is mixed with C_3S before hydration, the induction time increases to levels similar to those observed in cementitious pore solutions (see SI, Table S8 and Fig. S51). This indicates that sulfate ions play a significant role in inhibiting CH precipitation.

To further investigate the suspected inhibitory effect of sulfate ions, we conducted an additional series of precipitation experiments at 45 °C, a temperature at which gypsum is more soluble than at room temperature, thereby preventing gypsum precipitation. In this experiment series, we manipulated the sulfate concentration in the separated pore solutions by adding alkali sulfates (Na_2SO_4 and K_2SO_4 in a 1:7 molar ratio) to increase sulfate levels and by precipitating $BaSO_4$ with $BaCl_2{\cdot}2H_2O$ to decrease sulfate levels. This method is almost perfectly selective for the removal of SO_4^{2-} and allowed us to adjust the sulfate concentration of the separated pore solution from 1000 to 3500 mg/L (see SI, Table S5 and Fig. S48). It was not possible to increase the sulfate concentration indefinitely, as doing so would cause gypsum to precipitate instead of portlandite. Even with a moderate increase in sulfate concentration (+30 mmol/L), gypsum began to co-precipitate (see Table 1 and SI, Figs. S43, S58, S66, and S74), whereas at lower sulfate concentrations, only portlandite precipitated (see Table 1 and SI, Figs. S44, S59, S67, and S75). The conductivity measurements and induction times for CH precipitation are presented in Fig. 8 (and SI, Table S9). Due to the presence of additional alkali or chloride ions in solution, the measured conductivity in all experiments was higher than in the reference measurement (82 mmol/L). The induction time for CH precipitation from a cementitious pore solution shows an almost perfectly exponential relationship with sulfate concentration, clearly indicating that present sulfate ions inhibit CH nucleation in these solutions. However, since an induction period of 8 h for CH precipitation was also observed in a pure C_3S pore solution (see SI, Table S8 and Fig. S51)—where no sulfate ions are present—sulfate inhibition alone cannot fully account for the kinetic barrier to CH nucleation, suggesting that additional ionic species contribute to the observed metastability. The "silicate-poisoning theory" suggests that the crystallization of portlandite is also inhibited due to the poisoning of small crystallization nuclei by silicate species present in the pore solution[18–20].

We isolated the precipitates from the nucleation experiments and characterized them using TGA-MS, PXRD, FTIR (see SI, Sections S6–S8), and SEM (see SI, Section S3.3). Crystalline CH formed as a precipitate in all experiments when the pore solution was separated after 15 min or later and stirred under a nitrogen atmosphere (see Table 1, Fig. 7c and SI, Figs. S42, S56, S64, and S72). However, when the pore solution was separated directly 1 min after water addition, only gypsum was found, with no CH present (see Table 1 and SI, Figs. S39, S53, S61, and S69). In some cases, the presence of amorphous calcium carbonate (ACC) was detected, which is likely a result of inadvertent carbonation of the cementitious pore solution by atmospheric CO_2 due to contact with the air[67]. The SEM images (see Fig. 7d and SI, Fig. S41) of the isolated CH precipitates revealed flat hexagonal plates with sheet-like morphology. The observed crystals had edge lengths ranging from 1 to 10 µm and an average thickness of 0.5 µm. The diameter of fully developed portlandite crystals grown under controlled experimental

Table 1 | Proportions of portlandite and gypsum in isolated precipitates from precipitation experiments conducted on cementitious pore solutions at various temperatures (*T*), which were separated at different times after the start of hydration (t_{sep}) and had varying sulfate concentrations ($c(SO_4^{2-})$)

T [°C]	t_{sep} [min]	$c(SO_4^{2-})$ [mmol/L]	Portlandite [wt%]	Gypsum [wt%]
25	1	105	0	100
25	15	88	71	29
25	60	81	100	0
45	15	32	100	0
45	15	110	92	8
50	15	88	100	0

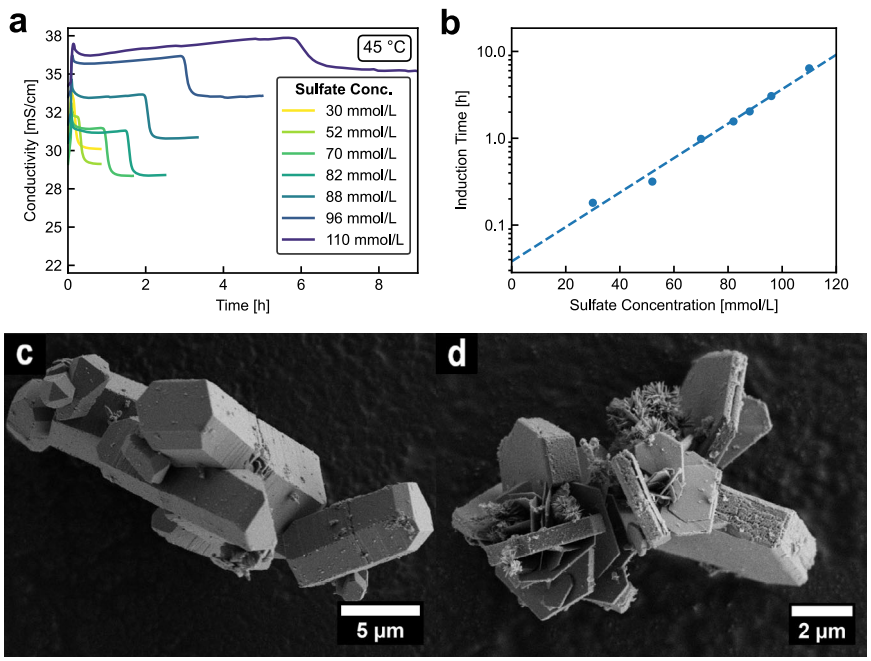


Fig. 8 | Dependence of the induction time for CH precipitation from cementitious pore solution on the sulfate concentration of the solution. **a** Conductivity measured over time at 45 °C of pore solutions separated 15 min after the start of hydration, with varying concentrations of sulfate ions in the solution. **b** Exponential relationship between the induction times for CH precipitation from the pore solution and the sulfate concentration. SEM images of the isolated precipitates at the lowest sulfate concentration of 30 mmol/L (**c**), and at the highest sulfate concentration of 110 mmol/L (**d**). Scale bars represent 5 and 2 µm, respectively.

Table 2 | Chemical composition of the technical OPC CEM I 42.5 N determined by ICP-OES analysis (LOI = loss on ignition), and the quantitative phase content determined by Rietveld refinement of PXRD data

Oxide	wt%	Phase	wt%
CaO	61.56	Alite	51.9
SiO_2	18.61	Belite	16.6
Al_2O_3	4.92	C_3A	8.6
SO_3	3.63	C_4AF	7.0
MgO	3.06	Anhydrite	4.4
Fe_2O_3	3.01	Calcite	3.1
K_2O	1.16	Periclase	2.5
TiO_2	0.30	Portlandite	2.2
P_2O_5	0.24	Syngenite	1.3
Na_2O	0.21	Arcanite	0.7
SrO	0.15	Bassanite	0.5
MnO	0.05	Aphthitalite	0.4
ZnO	0.03	Dolomite	0.3
BaO	0.02	Quartz	0.3
Cr_2O_3	0.01	Lime	0.2
V_2O_5	0.01	Gypsum	0.1
LOI	3.00		
Sum	99.97	Sum	99.9

Table 3 | Particle size distribution and specific surface area of the technical OPC CEM I 42.5 N

Parameter	Value
d_{10} [µm]	1.24
d_{50} [µm]	19.88
d_{90} [µm]	60.73
Blaine [cm^2/g]	3072

conditions typically ranges from 2 to 10 µm, while their length varies from 10 to 50 µm[43]. The size, shape, and habit of the obtained CH crystals are thus similar to those found in cement pastes[68], but differ considerably from those crystallizing in pure supersaturated CH solutions prepared by mixing $CaCl_2$ with NaOH[42,69,70]. The crystal morphology of CH is influenced by the ions present in the pore solution. Sulfate anions, for example, typically promote the formation of CH crystals with a c/a crystal axis ratio of less than 0.5[71]. This transformation of the crystal habit from prismatic to tabular, induced by additives such as sulfates, is clearly illustrated by comparing SEM images of the precipitates at the highest and lowest sulfate concentrations (see Fig. 8 and SI, Figs. S43 and S44). Additionally, SEM images of precipitates from the C_3S pore solutions further demonstrate this change. When gypsum is mixed with C_3S before hydration, portlandite precipitates as flat hexagonal plates (see SI, Fig. S46) rather than elongated prismatic columns or very thin plate-like crystals (see SI, Fig. S45) from the separated pore solution.

In nucleation experiments conducted in air rather than an inert gas, a colorless precipitate formed quickly (within minutes) at the liquid-gas interface, identified as calcite through TGA-MS, PXRD, and FTIR analyses (see SI, Figs. S57, S65, and S73). Electron micrographs of separated pore solution exposed to air for 1 day revealed stacks of crystalline particles with the characteristic shape of calcite (see SI, Fig. S27). The initially spherical ACH particles transformed into crystalline calcium carbonate. The ACH particles are only metastable under an inert gas atmosphere and exhibit high reactivity towards atmospheric CO_2, as demonstrated by EELS measurements (see Fig. 1 and SI, Fig. S28). Based on our findings, particularly the EELS measurements, we hypothesize that this transformation occurs via an intermediate ACC stage. Guzmán García Lascurain et al. also detected ACC in their ex situ analysis of microcellulose-stabilized ACH, likely due to accidental carbonation of the ACH during sample preparation in air[45].

Conclusions

In summary, we provide insights into the native state of CH and its crystallization pathways in cementitious pore solutions.

We detected and analyzed large spherical ACH particles (up to 1 µm) using conventional TEM and showed that they form during drying of the pore solution on a TEM grid. The sample preparation method critically governs the size, shape, and agglomeration state of the observed particles: blotting produces spherical particles approximately 100 nm in size, drop casting yields smaller agglomerated species below 20 nm, and ethanol quenching introduces additional solvent-induced structures. The spherical ACH particles reported in earlier publications on hydrating C_3S surfaces[29–31] can thus likely be attributed to similar preparation artifacts.

Cryo-HRTEM, SAXS, and PDF analysis revealed no evidence of CH precursor species above the detection limit, consistent with CH being present as fully solvated ions or ion pairs in the cementitious pore solution separated after 15 min. The only particulate species detected in the native pore solution are metastable gypsum prenucleation clusters of approximately 1 nm in diameter. Furthermore, the isolated cementitious pore solution remains metastable for several days under inert, low-temperature conditions, and portlandite precipitates only upon heating or evaporation, with the induction time depending on both the temperature and the timing of separation (i.e., the chemical composition) of the pore solution. This metastability is primarily caused by the inhibitory effects of several ions in the pore solution, particularly sulfates and silicates, on CH precipitation. Moreover, only portlandite (along with gypsum in the very early stage) crystallizes from a separated cementitious pore solution, whereas no C-S-H, ettringite, or any other hydrate phase does.

Our observations confirm that both CH and calcium sulfate crystallize from cementitious pore solutions via "non-classical" pathways, though their crystallization routes appear fundamentally different. While calcium sulfate forms prenucleation clusters in solution, CH remains fully dissolved until nucleation is triggered. Once initiated, CH crystallization proceeds through a multi-stage process: dissolved ions associate into clusters, which coalesce into amorphous spherical nanoparticles, aggregate into networks, and ultimately transform into hexagonal portlandite crystals with the morphology characteristic of cementitious systems. These findings confirm the validity of "non-classical" nucleation pathways in Portland cement hydration and significantly advance our understanding of portlandite and gypsum formation during the early stages of cement hydration.

Methods

The following sections outline the materials and methods used in this study, as well as the experiments conducted. Detailed procedural descriptions for OPC analysis, ICP-OES, PXRD, TGA-MS, FTIR, and isothermal heat flow calorimetry, along with their corresponding results, are provided in the Supplementary Information.

Materials

Ultrapure water (DI-H_2O, NANOpure Diamond, Barnstead) and ordinary Portland cement (OPC) CEM I 42.5 N were utilized for all hydration experiments. The chemical composition of the OPC was determined by ICP-OES analysis after dissolution with HF, and the quantitative phase content through Rietveld refinement of PXRD data (see Table 2, and SI, Section S1 for experimental details). Characteristic particle distributions were obtained on a CILAS 1064 laser granulometer (*Cilas*, Orléans, France), and the Blaine value using a Blaine apparatus according to EN 196-6 (see Table 3). Tricalcium silicate (C_3S) was prepared using a protocol developed

by Li et al.[72]. All other chemicals were purchased from commercial suppliers and used as received without further purification.

Cement paste preparation

We mixed technical Portland cement (CEM I 42.5 N) with ultrapure water at a water-to-cement ratio (*w/c*) of 1.0 without adding any additives. The high *w/c* ratio was intentionally chosen to facilitate rapid separation via dead-end filtration and to ensure an adequate solution volume for subsequent nucleation experiments (the stainless-steel pressure filter holder has a maximum volume of 200 mL). The cement pastes were prepared by adding 130 g of OPC to 130 g DI-H_2O (*w/c* = 1.0) in a 250 mL polyethene cup over a period of 10 s. The paste was then mixed for 1 min using an overhead stirrer (*IKA* Nanostar 20 digital, Staufen, Germany) equipped with a four-blade propeller at 500 rpm. Afterward, the plastic cup containing the cement paste was sealed with a plastic lid. Fourteen minutes after the first water contact, the cement paste was stirred again for 1 min at 500 rpm.

Pore solution separation by dead-end filtration

After 15 min, once the initial ettringite formation had subsided, we separated the pore solution from the cement paste using dead-end filtration. The separated pore solution was then analyzed by pH and ICP-OES measurements (see SI, Table S4) in addition to examination under the TEM (see SI, Section S1). The cement paste was filled into a stainless steel cylinder with a volume of 200 mL equipped with a poly(ether sulfone) (PES) 0.45 µm membrane filter (both by *Sartorius Stedim Biotech GmbH*, Göttingen, Germany). Afterward, air pressure was applied to the steel cylinder. The filtrate was collected for 2 min after the application of pressure. TEM and ICP-OES samples were prepared immediately from the obtained filtrate—the total sample preparation time after pressure application was approximately 5 min. The pH of the separated pore solution was subsequently measured using a pH electrode (InLab Micro Pro-ISM) connected to a FiveEasy pH meter (both from *Mettler Toledo*, Greifensee, Switzerland). The pH electrode was calibrated beforehand using three standard buffers at pH 6.865, 9.180, and 12.454 (*Mettler Toledo*, Greifensee, Switzerland). In some experiments, the cementitious pore solution was separated by centrifugation[50] or continuous cross-flow filtration[51]. The detailed experimental methods are described in the referenced literature[50,51]. In addition, we also isolated C_3S pore solutions for the ethanol quenching experiments using the described dead-end filtration method.

Transmission electron microscopy (TEM)

TEM sample preparation methods. The TEM samples were prepared using four different methods: (1) drop casting, (2) blotting, (3) EtOH quenching, and (4) cryo-TEM preparation. The experimental details are provided below. An overview of the methods employed is also shown in the Supplementary Information (see SI, Fig. S1).

1) Drop casting: 10 µL of the separated pore solution was dropped onto a carbon layer-covered copper TEM grid (*Micro to Nano*, Carbon Film on Copper, 300 Mesh) placed on a filter paper. Excess liquid was immediately drawn up by the underlying filter paper. The TEM grid was then left to dry overnight in a Petri dish.
2) Blotting: 10 µL of the separated pore solution was carefully placed on a carbon layer-covered copper TEM grid (*Micro to Nano*, Carbon Film on Copper, 300 Mesh). Excess water was removed after 1 min by blotting with filter paper, and the TEM grid was then dried overnight in the air.
3) EtOH quenching: immediately after separation of the pore solution (within a minute), EtOH was added to the solution at a 1:10 volume ratio. The TEM grid was then prepared with this solution using the same procedure as for blotting.
4) Cryo-TEM preparation: for the cryo-TEM measurements, 5 µL of the separated pore solution was deposited using a volumetric pipette on lacey carbon grids (Quantifoil R 2/1 on 300 copper mesh), which were pre-treated by glow discharge (GloQube Plus, *Quorum Technologies*, Laughton (East Sussex), UK) for 30 s and subsequently equilibrated at 15 °C and 95% relative humidity. The solution droplet on the grid was then blotted five times and plunged into a liquid ethane/propane mixture (3:1 by volume) using an automated plunge freezer Vitrobot Mark IV (*Thermo Fisher Scientific*, Waltham, MA, USA). The blotting parameters were: blot time: 6 s, wait time: 0 s, drain time: 0 s, blot force: 8, total blotting: 5. The resulting vitrified thin films were stored in liquid nitrogen until transferred to the cryo-TEM microscope.

For the cryo-HRTEM measurements, a smaller droplet of the pore solution (3 µL) was rapidly transferred to a glow discharge pretreated lacey carbon grid at 5 °C and 95% relative humidity. The small droplet was immediately blotted only once with lower contact pressure and for a shorter duration, before being plunged directly into a liquid ethane/propane mixture (3:1 by volume). The blotting parameters were: blot time: 4 s, wait time: 0 s, drain time: 0 s, blot force: 4, total blotting: 1. Compared with the cryo-TEM preparation, the reduced blotting intensity was intentionally chosen to minimize the contact time between the pore solution and the filter paper, thereby limiting partial drying of the thin liquid film before vitrification and reducing the driving force for ACH particle growth during sample preparation. All cryo-HRTEM imaging was performed exclusively in areas of vitreous ice within the holes of the lacey carbon film—regions that were not in contact with the filter paper during blotting and therefore remained continuously submerged in an aqueous layer throughout sample preparation.

TEM imaging and analysis. Conventional TEM measurements were performed on a *JEOL* JEM-1400plus transmission electron microscope (*JEOL*, Akishima, Tokyo, Japan) operating at 120 kV, equipped with a LaB_6 electron source and a RUBY CCD camera.

The selected area electron diffraction (SAED) and electron energy loss spectroscopy (EELS) measurements were conducted on a *JEOL* JEM-F200 transmission electron microscope (*JEOL*, Akishima, Tokyo, Japan) equipped with a Gatan Continuum GIF spectrometer and a K3 post filter direct electron detection camera. The EELS spectra were recorded in scanning transmission electron microscopy mode (STEM) with a zero-loss energy resolution of 0.6 eV at full width at half maximum and an energy dispersion of 0.1 eV per channel.

Cryo-prepared specimens were imaged at −180 °C using a "Glacios" cryo-TEM (*Thermo Fisher Scientific*, Waltham, MA, USA) equipped with a Falcon 4i direct electron detector at an acceleration voltage of 200 kV.

The cryo-HRTEM measurements were conducted at −180 °C on a TEM Cs-corrected Titan Krios G2 microscope (*Thermo Fisher Scientific*, Waltham, MA, USA) equipped with a Falcon III direct electron detector at an acceleration voltage of 300 kV.

Precipitation experiments

After separation by dead-end filtration, the cementitious pore solution was transferred to a 100 mL double-walled glass reactor under a nitrogen atmosphere. The conductivity of the separated pore solution was measured using an InLab 731-ISM conductivity electrode (*Mettler Toledo*, Greifensee, Switzerland) connected to an ALMEMO 104 datalogger (*Ahlborn Mess- und Regelungstechnik GmbH*, Holzkirchen, Germany). Before each precipitation experiment, the glass reactor was cleaned with 10% acetic acid. The measurements were performed over time under magnetic stirring (300 rpm) and a gentle flow of nitrogen at a defined temperature, which was maintained using an external refrigerated/heated circulator CORIO CD-200F (*Julabo GmbH*, Seelbach, Germany). The measured conductivity values were recorded at intervals of 60 s. The measurements were stopped after a precipitate had formed and the conductivity had reached a constant value after it had dropped. The precipitate was separated from the solution by centrifugation at 8500 rpm for 5 min (Biofuge primo R, *Heraeus*, Hanau, Germany) and washed with 10 mL of a saturated CH solution and isopropyl alcohol. Afterward, it was dried under a nitrogen stream and stored in a nitrogen atmosphere until further analysis. The precipitate was characterized by TGA-MS, PXRD, FTIR, and SEM. Procedural details for the TGA-

MS, PXRD, and FTIR methods are provided in the Supplementary Information.

To determine how the induction time depends on the sulfate concentration of the pore solution, the sulfate concentration of the solution was adjusted immediately after dead-end filtration, but before starting the conductivity measurement. To increase the sulfate level, alkali sulfates were added after separation. The Na_2SO_4-to-K_2SO_4 ratio (1:7 molar ratio) was selected to maintain the sodium-to-potassium ratio in the pore solution largely unchanged. To decrease the sulfate level, part of the sulfate was precipitated as $BaSO_4$ by adding $BaCl_2{\cdot}2H_2O$. This process required an immediate secondary filtration of the pore solution to fully separate the $BaSO_4$ precipitate. The conductivity measurements at 45 °C, along with the isolation and characterization of the precipitates, were then performed as described above.

Additional precipitation experiments were conducted at 25 °C using a pure C_3S pore solution and a pore solution derived from a C_3S-gypsum mixture at a 95:5 weight ratio.

Scanning electron microscopy (SEM)

The formation of ACH from cementitious pore solution was also studied using scanning electron microscopy (SEM). The pore solution was separated through dead-end filtration 15 min after the start of cement hydration. 10 µL of the separated pore solution was then applied to a TEM grid or a silicon wafer, and the excess liquid was blotted away with filter paper before the surface was allowed to dry in the air. Instead of imaging the sample under the TEM, we mounted the TEM grid or silicon wafer on a suitable SEM sample holder using double-sided carbon tape.

Additionally, we examined the crystalline precipitates from the nucleation experiments using SEM. A small amount of an isolated precipitate was mounted on a specimen holder for SEM analysis using double-sided carbon tape. The preparation was conducted in air at room temperature without any additional coating of the sample.

Images were captured under vacuum with a Zeiss Supra 50 VP FE-SEM (*Carl Zeiss AG*, Oberkochen, Germany) operating with a primary electron beam energy of 3 kV and beam deceleration mode at a 5 kV stage bias. An Everhart–Thornley detector (ETD) was used for imaging. Energy dispersive X-ray spectroscopy (EDX) measurements were performed using an EDAX Octane Elite Ultra EDS/EDX system (*Amatek Inc*., Berwyn, PA, USA) at an acceleration voltage of 10 kV.

Small-angle X-ray scattering (SAXS)

SAXS experiments were performed using a laboratory-based SAXS-WAXS beamline, KWS-X (*Xenocs* Xuess 3.0 XL, Grenoble, France) at Jülich Centre for Neutron Science (*JCNS-MLZ*, Garching, Germany). The Metal-Jet X-ray source (*Excillum* MetalJet D2+, Kista, Sweden) with a liquid metal anode was operated at 70 kV and 3.57 mA, emitting Ga-K_α radiation with a wavelength of $\lambda = 1.314$ Å. All samples were measured in sealed 2 mm glass capillaries, and the sample-to-detector distances varied from 0.65 to 1.7 m. The SAXS patterns were normalized to an absolute scale and azimuthally averaged to produce one-dimensional intensity profiles, with the water background subtracted.

Pair distribution function (PDF)

Total scattering measurements were performed at beamline ID31 at the European Synchrotron Radiation Facility (ESRF). The sample was applied to cylindrical slots (approximately 1 mm thick) held between Kapton windows in a high-throughput sample holder. Each sample was measured in transmission geometry with an incident X-ray energy of 75.051 keV ($\lambda = 0.16520$ Å). Measured intensities were collected using a Pilatus CdTe 2M detector positioned with the incident beam in the corner of the detector. The sample-to-detector distance was approximately 0.3 m for the total scattering measurements.

NIST SRM 660b (LaB_6) was used for geometry calibration. Integration was performed using the software pyFAI, including flat-field, geometry, solid-angle, and polarization corrections. Invalid pixels were masked, and the sigma clipping integration algorithm was used to automask further azimuthal outliers. The summed background intensities were scaled to each of the reference and sample measurements and then subtracted. Rietveld refinements were performed using TOPAS V7[73] to fit the structure with the reference lattice parameter fixed to the measurement to determine the instrumental profile contribution and correct for offset errors, including parallax[74].

Preliminary PDF data were processed in an automated way using PDFgetX3 for a range of Q_{max} values[75]. Then the data were reprocessed using a Lorch modification function to suppress termination effects and contributions from high-frequency noise[76]. The small-angle scattering intensities were extrapolated from $Q_{min} \sim 0.1$ Å^{-1} to 0.

Data availability

The data generated and analyzed in this study are included in the published article and its supplementary information file. The electron micrographs shown and the raw measurement data are available in the Zenodo repository at https://doi.org/10.5281/zenodo.21246562. Further data are available from the corresponding author upon reasonable request.

Received: 23 January 2026; Accepted: 10 August 2026;
Published online: 04 September 2026

References

1. Bhatty, J. I. (ed.) *Innovations in Portland Cement Manufacturing* (PCA Portland Cement Association, 2011).
2. Yang, K.-H., Cho, A.-R., Song, J.-K. & Nam, S.-H. Hydration products and strength development of calcium hydroxide-based alkali-activated slag mortars. *Constr. Build. Mater.* **29**, 410–419 (2012).
3. Vance, K. et al. Direct carbonation of $Ca(OH)_2$ using liquid and supercritical CO_2 : implications for carbon-neutral cementation. *Ind. Eng. Chem. Res.* **54**, 8908–8918 (2015).
4. Blamey, J., Lu, D. Y., Fennell, P. S. & Anthony, E. J. Reactivation of CaO-based sorbents for CO_2 capture: mechanism for the carbonation of $Ca(OH)_2$. *Ind. Eng. Chem. Res.* **50**, 10329–10334 (2011).
5. Xie, Q., Wan, L., Zhang, Z. & Luo, J. Electrochemical transformation of limestone into calcium hydroxide and valuable carbonaceous products for decarbonizing cement production. *iScience* **26**, 106015 (2023).
6. Oates, J. A. H. *Lime and Limestone: Chemistry and Technology, Production and Uses* (Wiley-VCH, 2008).
7. Bullard, J. W. & Flatt, R. J. New insights into the effect of calcium hydroxide precipitation on the kinetics of tricalcium silicate hydration. *J. Am. Ceram. Soc.* **93**, 1894–1903 (2010).
8. Taylor, H. *Cement Chemistry* (Thomas Telford Publishing, 1997).
9. Hu, Q. et al. Direct three-dimensional observation of the microstructure and chemistry of C_3S hydration. *Cem. Concr. Res.* **88**, 157–169 (2016).
10. Banfill, P. F. G. Precipitation of calcium hydroxide in the presence of organic compounds. *J. Mater. Sci. Lett.* **5**, 33–34 (1986).
11. Yan, Y. & Geng, G. Evolution of C-S-H morphology at early age: new insights from direct TEM observation. *J. Build. Eng.* **73**, 106764 (2023).
12. Fylak, M. J. *Untersuchungen zum frühen Hydratationsverhalten von Portland- und Portlandkompositzementen*. Dissertation, Martin-Luther-Universität Halle-Wittenberg (2011).
13. Morales-Cantero, A., Cuesta, A., Santacruz, I., Aranda, M. A. & de La Torre, A. G. Phase-selective degree of hydration at setting: an in situ synchrotron diffraction study. *Constr. Build. Mater.* **328**, 127117 (2022).
14. Young, J. F., Tong, H. S. & Berger, R. L. Compositions of solutions in contact with hydrating tricalcium silicate pastes. *J. Am. Ceram. Soc.* **60**, 193–198 (1977).
15. Remus, R., Rößler, C., Peters, S., Sowoidnich, T. & Ludwig, H.-M. Fundamental effects of using power ultrasound to accelerate C_3S hydration. *Cem. Concr. Res.* **180**, 107514 (2024).

16. Sowoidnich, T. *A Study of Retarding Effects on Cement and Tricalcium Silicate Hydration Induced by Superplasticizers*. Dissertation, Bauhaus-Universität Weimar (2015).
17. Lothenbach, B. & Nonat, A. Calcium silicate hydrates: solid and liquid phase composition. *Cem. Concr. Res.* **78**, 57–70 (2015).
18. Tadros, M. E., Skalny, J. A. & Kalyoncu, R. S. Early hydration of tricalcium silicate. *J. Am. Ceram. Soc.* **59**, 344–347 (1976).
19. Wu, Z.-Q. & Young, J. F. Formation of calcium hydroxide from aqueous suspensions of tricalcium silicate. *J. Am. Ceram. Soc.* **67**, 48–51 (1984).
20. Galmarini, S., Kunhi Mohamed, A. & Bowen, P. Atomistic simulations of silicate species interaction with portlandite surfaces. *J. Phys. Chem. C* **120**, 22407–22413 (2016).
21. Yan-Rong, Z. et al. Influence of triethanolamine on the hydration product of portlandite in cement paste and the mechanism. *Cem. Concr. Res.* **87**, 64–76 (2016).
22. Grangeon, S. et al. Quantitative X-ray pair distribution function analysis of nanocrystalline calcium silicate hydrates: a contribution to the understanding of cement chemistry. *J. Appl. Crystallogr.* **50**, 14–21 (2017).
23. Groves, G. W. Microcrystalline calcium hydroxide in Portland cement pastes of low water/cement ratio. *Cem. Concr. Res.* **11**, 713–718 (1981).
24. Groves, G. W. & Richardson, I. G. Microcrystalline calcium hydroxide in pozzalanic cement pastes. *Cem. Concr. Res.* **24**, 1191–1196 (1994).
25. Bache, H. H., Idorn, G. M., Nepper-Christensen, P. & Nielsen, J. Morphology of calcium hydroxide in cement paste. In *Proc. Highway Research Board Special Report*, Vol. 90, 154–174 (Highway Research Board, 1966).
26. Milestone, N. B. Hydration of tricalcium silicate in the presence of lignosulfonates, glucose, and sodium gluconate. *J. Am. Ceram. Soc.* **62**, 321–324 (1979).
27. Odler, I. & Dörr, H. Early hydration of tricalcium silicate I. Kinetics of the hydration process and the stoichiometry of the hydration products. *Cem. Concr. Res.* **9**, 239–248 (1979).
28. Odler, I. & Dörr, H. Early hydration of tricalcium silicate II. The induction period. *Cem. Concr. Res.* **9**, 277–284 (1979).
29. Midgley, H. G. The determination of calcium hydroxide in set Portland cements. *Cem. Concr. Res.* **9**, 77–82 (1979).
30. Ings, J. B., Brown, P. W. & Frohnsdorff, G. Early hydration of large single crystals of tricalcium silicate. *Cem. Concr. Res.* **13**, 843–848 (1983).
31. Ménétrier, D., Jawed, I., Sun, T. S. & Skalny, J. ESCA and SEM studies on early C_3S hydration. *Cem. Concr. Res.* **9**, 473–482 (1979).
32. Rheinheimer, V. *A Nanoscale Study of Dissolution and Growth Processes in Cement Hydrates*. Dissertation, Universitat Politècnica de Catalunya (2012).
33. Rheinheimer, V. & Casanova, I. Hydration of C_3S thin films. *Cem. Concr. Res.* **42**, 593–597 (2012).
34. Beaudoin, J. & Odler, I. Hydration, setting and hardening of Portland cement. in (eds Hewlett, P. C., Liška, M. & Lea, F. M.) *Lea's Chemistry of Cement and Concrete*, 157–250 (Elsevier, 2019).
35. Ruiz-Agudo, C. & Cölfen, H. Exploring the potential of nonclassical crystallization pathways to advance cementitious materials. *Chem. Rev.* **124**, 7538–7618 (2024).
36. Krautwurst, N. et al. Two-step nucleation process of calcium silicate hydrate, the nanobrick of cement. *Chem. Mater.* **30**, 2895–2904 (2018).
37. Sowoidnich, T. et al. The nucleation of C-S-H via prenucleation clusters. *J. Chem. Phys.* **158**, 114309 (2023).
38. Aretxabaleta, X. M., López-Zorrilla, J., Etxebarria, I. & Manzano, H. Multi-step nucleation pathway of C-S-H during cement hydration from atomistic simulations. *Nat. Commun.* **14**, 7979 (2023).
39. Rieger, J. et al. Precursor structures in the crystallization/ precipitation processes of $CaCO_3$ and control of particle formation by polyelectrolytes. *Faraday Discuss.* **136**, 265–277 (2007).
40. Gebauer, D., Völkel, A. & Cölfen, H. Stable prenucleation calcium carbonate clusters. *Science* **322**, 1819–1822 (2008).
41. Rodriguez-Navarro, C., Ruiz-Agudo, E., Burgos-Cara, A., Elert, K. & Hansen, E. F. Crystallization and colloidal stabilization of $Ca(OH)_2$ in the presence of nopal juice (*Opuntia ficus indica*): implications in architectural heritage conservation. *Langmuir* **33**, 10936–10950 (2017).
42. Rodriguez-Navarro, C., Burgos-Cara, A., Di Lorenzo, F., Ruiz-Agudo, E. & Elert, K. Nonclassical crystallization of calcium hydroxide via amorphous precursors and the role of additives. *Cryst. Growth Des.* **20**, 4418–4432 (2020).
43. Madeja, B. et al. New insights into the nucleation of portlandite and the effects of polymeric additives. *Cem. Concr. Res.* **173**, 107258 (2023).
44. Kang, S.-H., Kwon, M., Kwon, Y.-H. & Moon, J. Effects of polycarboxylate ether (PCE)-based superplasticizer on the dissolution and subsequent hydration of calcium oxide (CaO). *Cem. Concr. Res.* **146**, 106467 (2021).
45. Guzmán García Lascurain, P., Rodriguez-Navarro, C., Toniolo, L. & Goidanich, S. Effects of nano- and micro-cellulose on $Ca(OH)_2$ formation: implications for lime-based binders. *Cem. Concr. Res.* **192**, 107851 (2025).
46. Ylmén, R., Jäglid, U., Steenari, B.-M. & Panas, I. Early hydration and setting of Portland cement monitored by IR, SEM and Vicat techniques. *Cem. Concr. Res.* **39**, 433–439 (2009).
47. Scrivener, K., Snellings, R. & Lothenbach, B. (eds.) *A Practical Guide to Microstructural Analysis of Cementitious Materials* (CRC Press, 2017).
48. Vollpracht, A., Lothenbach, B., Snellings, R. & Haufe, J. The pore solution of blended cements: a review. *Mater. Struct.* **49**, 3341–3367 (2016).
49. Dengler, J. E., Grassl, H., Bizzozero, J. & Gädt, T. Analysis of cementitious pore solutions with very high time resolution by coupling cross flow filtration and ICP-OES. *Mater. Today Commun.* **39**, 109095 (2024).
50. Rindle, O., Sixt, F., Spillane, L., Willinger, E. & Gädt, T. Revealing the morphology of nano-ettringite in cement paste: a TEM study on the influence of polycarboxylate ether superplasticizers. *Cem. Concr. Res.* **193**, 107853 (2025).
51. Nickl, S. et al. Investigating the evolution of the cementitious pore solution during the first 15 minutes of hydration via dynamic crossflow filtration. *CEMENT* **24**, 100181 (2026).
52. Caruso, F., Mantellato, S., Palacios, M. & Flatt, R. J. ICP-OES method for the characterization of cement pore solutions and their modification by polycarboxylate-based superplasticizers. *Cem. Concr. Res.* **91**, 52–60 (2017).
53. van Driessche, A., Stawski, T. M. & Kellermeier, M. Calcium sulfate precipitation pathways in natural and engineered environments. *Chem. Geol.* **530**, 119274 (2019).
54. Kellermeier, M. et al. From ions to crystals: a comprehensive view of the non-classical nucleation of calcium sulfate. *Angew. Chem. Int. Ed.* **63**, e202408429 (2024).
55. Ilett, M. et al. Studying crystallisation processes using electron microscopy: the importance of sample preparation. *J. Microsc.* **295**, 243–256 (2024).
56. Gallucci, E. & Scrivener, K. Crystallisation of calcium hydroxide in early age model and ordinary cementitious systems. *Cem. Concr. Res.* **37**, 492–501 (2007).
57. Diamond, S. Calcium hydroxide in cement paste and concrete —a microstructural appraisal. in (eds Skalny, J. P., Gebauer, J. & Odler, I.) *Materials Science of Concrete, Special Volume*, 37–58 (John Wiley & Sons, 2001).

58. Diamond, S. The microstructure of cement paste and concrete—a visual primer. *Cem. Concr. Compos.* **26**, 919–933 (2004).
59. Williamson, R. B. Solidification of Portland cement. *Prog. Mater. Sci.* **15**, 189–286 (1972).
60. Gebauer, D., Kellermeier, M., Gale, J. D., Bergström, L. & Cölfen, H. Pre-nucleation clusters as solute precursors in crystallisation. *Chem. Soc. Rev.* **43**, 2348–2371 (2014).
61. Stawski, T. M. et al. Formation of calcium sulfate through the aggregation of sub-3 nanometre primary species. *Nat. Commun.* **7**, 11177 (2016).
62. Baken, A. et al. Additive-specific modulation of non-classical nucleation pathways. *Nat. Commun.* **17**, 1925 (2026).
63. Brisard, S., Davy, C. A., Michot, L., Troadec, D. & Levitz, P. Mesoscale pore structure of a high–performance concrete by coupling focused ion beam/scanning electron microscopy and small angle X–ray scattering. *J. Am. Ceram. Soc.* **102**, 2905–2923 (2019).
64. Beaucage, G. Small-angle scattering from polymeric mass fractals of arbitrary mass-fractal dimension. *J. Appl. Crystallogr.* **29**, 134–146 (1996).
65. Kotlarchyk, M. & Chen, S.-H. Analysis of small angle neutron scattering spectra from polydisperse interacting colloids. *J. Chem. Phys.* **79**, 2461–2469 (1983).
66. Stawski, T. M. et al. The structure of $CaSO_4$ nanorods: the precursor of gypsum. *J. Phys. Chem. C* **123**, 23151–23158 (2019).
67. Monkman, S., Lee, B. E., Grandfield, K., MacDonald, M. & Raki, L. The impacts of in-situ carbonate seeding on the early hydration of tricalcium silicate. *Cem. Concr. Res.* **136**, 106179 (2020).
68. Franus, W., Panek, R. & Wdowin, M. SEM investigation of microstructures in hydration products of Portland cement. In *Proc. 2nd International Multidisciplinary Microscopy and Microanalysis Congress* (eds Polychroniadis, E. K., Oral, A. Y. & Ozer, M.) Vol. 164 of *Springer Proceedings in Physics*, 105–112 (Springer International Publishing, 2015).
69. Vohburger, A., Collin, M., Bouissonnié, A., Nicoleau, L. & Gädt, T. Citric, tartaric, and succinic acid effects on C_3S dissolution and the nucleation kinetics of C-S-H and portlandite. *Cem. Concr. Res.* **197**, 107964 (2025).
70. Vohburger, A., Collin, M., Rindle, O. & Gädt, T. Influence of polymeric dispersants on the dissolution rate of tricalcium silicate and the nucleation of calcium-silicate-hydrate and portlandite. *Chem. Eur. J.* **31**, e202500207 (2025).
71. Berger, R. L. & McGregor, J. D. Influence of admixtures on the morphology of calcium hydroxide formed during tricalcium silicate hydration. *Cem. Concr. Res.* **2**, 43–55 (1972).
72. Li, X., Ouzia, A. & Scrivener, K. Laboratory synthesis of C_3S on the kilogram scale. *Cem. Concr. Res.* **108**, 201–207 (2018).
73. Coelho, A. A. Topas and topas-academic : an optimization program integrating computer algebra and crystallographic objects written in C++. *J. Appl. Crystallogr.* **51**, 210–218 (2018).
74. Marlton, F. et al. A simple correction for the parallax effect in X-ray pair distribution function measurements. *J. Appl. Crystallogr.* **52**, 1072–1076 (2019).
75. Juhás, P., Davis, T., Farrow, C. L. & Billinge, S. J. L. PDFgetX3 : a rapid and highly automatable program for processing powder diffraction data into total scattering pair distribution functions. *J. Appl. Crystallogr.* **46**, 560–566 (2013).
76. Lorch, E. Neutron diffraction by germania, silica and radiation-damaged silica glasses. *J. Phys. C Solid State Phys.* **2**, 229–237 (1969).

Acknowledgements

The authors would like to express their gratitude to Carsten Peters (TUM Electron Microscopy Core Facility) for his assistance in preparing the cryo-TEM samples and to Christin Bauer (TUM) and Ali Rinaldi (TUM Electron Microscopy Core Facility) for the SEM measurements. We acknowledge the European Synchrotron Radiation Facility (ESRF) for providing synchrotron radiation facilities and Momentum Transfer for facilitating the measurements. We would like to thank Didier Blanchard (Momentum Transfer) for his assistance with data collection and Maxwell Terban (Momentum Transfer) for his contributions to data analysis. Jakub Drnec (ESRF) is thanked for assistance and support in using beamline ID31.

Author contributions

S.K. designed the research, conducted the experiments, collected, analyzed, and interpreted the data, and wrote the manuscript. E.W. performed cryo-HRTEM experiments, including EELS and SAED measurements, analyzed and interpreted the resulting data, and critically reviewed and revised the manuscript. B.W. conducted and evaluated the SAXS measurements and critically reviewed and revised the manuscript. T.G. funded and supervised the research project and critically reviewed and revised the manuscript. All authors have read and approved the final version of the manuscript submitted.

Funding

Open Access funding enabled and organized by Projekt DEAL.

Competing interests

The authors declare no competing interests.

Additional information

Supplementary information The online version contains supplementary material available at https://doi.org/10.1038/s43246-026-01339-y.

Correspondence and requests for materials should be addressed to Torben Gädt.

Peer review information *Communications Materials* thanks Christiane Rößler, Yuandong Mu, and the other anonymous reviewer(s) for their contribution to the peer review of this work. A peer review file is available.

Reprints and permissions information is available at http://www.nature.com/reprints

Publisher's note Springer Nature remains neutral with regard to jurisdictional claims in published maps and institutional affiliations.

Open Access This article is licensed under a Creative Commons Attribution 4.0 International License, which permits use, sharing, adaptation, distribution and reproduction in any medium or format, as long as you give appropriate credit to the original author(s) and the source, provide a link to the Creative Commons licence, and indicate if changes were made. The images or other third party material in this article are included in the article's Creative Commons licence, unless indicated otherwise in a credit line to the material. If material is not included in the article's Creative Commons licence and your intended use is not permitted by statutory regulation or exceeds the permitted use, you will need to obtain permission directly from the copyright holder. To view a copy of this licence, visit http://creativecommons.org/licenses/by/4.0/.

© The Author(s) 2026